Front. Energy 2021, 15(3): 710–720
https://doi.org/10.1007/s11708-021-0764-x

RESEARCH ARTICLE

Jiali DONG, Xuqiang ZHANG, Gongxuan LU, Chengwei WANG

Generation of enhanced stability of SnO/$In(OH)_3$/InP for photocatalytic water splitting by SnO protection layer

Abstract InP shows a very high efficiency for solar light to electricity conversion in solar cell and may present an expectation property in photocatalytic hydrogen evolution. However, it suffers serious corrosion in water dispersion. In this paper, it is demonstrated that the stability and activity of the InP-based catalyst are effectively enhanced by applying an anti-corrosion SnO layer and $In(OH)_3$ transition layer, which reduces the crystal mismatch between SnO and InP and increases charge transfer. The obtained Pt/SnO/$In(OH)_3$/InP exhibits a hydrogen production rate of 144.42 μmol/g in 3 h under visible light illumination in multi-cycle tests without remarkable decay, 123 times higher than that of naked $In(OH)_3$/InP without any electron donor under visible irradiation.

Keywords SnO/$In(OH)_3$/InP photocatalyst, enhanced activity and stability for water splitting, corrosion inhibition, enhancing charge transfer and decreasing crystal mismatch

Received Mar. 8, 2021; accepted May 27, 2021; online Jul. 30, 2021

Jiali DONG, Chengwei WANG (✉)
Key Laboratory of Atomic and Molecular Physics and Functional Materials of Gansu Province, College of Physics and Electronic Engineering, Northwest Normal University, Lanzhou 730070, China
E-mail: cwwang@nwnu.edu.cn

Xuqiang ZHANG
Key Laboratory of Atomic and Molecular Physics and Functional Materials of Gansu Province, College of Physics and Electronic Engineering, Northwest Normal University, Lanzhou 730070, China; State Key Laboratory for Oxo Synthesis and Selective Oxidation, Lanzhou Institute of Chemical Physics, Chinese Academy of Sciences, Lanzhou 730070, China

Gongxuan LU (✉)
State Key Laboratory for Oxo Synthesis and Selective Oxidation, Lanzhou Institute of Chemical Physics, Chinese Academy of Sciences, Lanzhou 730070, China
E-mail: gxlu@lzb.ac.cn

Special Issue—Photocatalysis: From Solar Light to Hydrogen Energy (Guest Editors: Wenfeng SHANGGUAN, Akihiko KUDO, Zhi JIANG, Yuichi YAMAGUCHI)

1 Introduction

Hydrogen is one of the cleanest renewable energy carriers, possibly replacing fossil fuels [1–6]. Hydrogen generation via photocatalytic water splitting can produce cheaper, clean, and renewable hydrogen driven by solar energy. Many semiconductor photocatalysts are found to be active for hydrogen evolution, such as CdS, ZnS [7,8], TiO_2, WO_3, ZnO [9–11], Ta_3N_5, GaN [12,13], and $Ni(OH)_2$, $In(OH)_3$ [14,15]. However, these catalysts can only absorb ultraviolet light or visible light shorter than 600 nm that accounts for less than 40% of the solar radiation on the earth. It is urgent to develop catalysts that can absorb longer wavelength visible light or infrared light for approaching effective use of solar energy, and catalyze water splitting to hydrogen with enough stability. At the same time, these catalysts have to hold suitable potential positions and good carrier mobilities for the reaction [16,17].

Since III-V semiconductors exhibit an excellently wide spectral response, absorption, and high charge mobility, the solar cell made of III-V semiconductors usually have a very high conversion efficiency from light to photocurrent [18–21]. Scientists have proposed that the III-V semiconductor materials are potential photocatalysts for water splitting. Lou and Lee suggest that a two-dimensional GeC/GaN heterostructural material might present excellent photocatalytic properties in which GaN and GeC monolayer are stacked together [19]. InP (1.34 eV) is a typical III-V semiconductor material whose band edge position is higher than the reduction potential of water. More importantly, its surface charge recombination is extremely low (170 cm/s) [22], leading to a higher carrier transfer efficiency. However, InP is unstable in many electrolyte solutions and undergoes chemical corrosion or photocorrosion. Therefore, it is necessary to construct a protection layer to stabilize InP in water dispersion [23]. Such a protection layer should exhibit a broadened spectral transmission window and permit the transfer of

photogenerated charges [24]. At present, InP/Cu: ZnS QDs and Zn-InP QDs and other InP-based composite materials have been used for photocatalytic reduction of H_2. However, these catalysts require the addition of sacrificial reagents to achieve a high photocatalytic activity [25,26]. SnO has a bandgap of 2.5–3.4 eV. It is a p-type wide bandgap semiconductor that allows visible light transmission and can be easily prepared under low-temperature conditions. Besides, it is very stable in water in the range of pH = 4–14 [27]. Nevertheless, due to the lattice matching problem between the semiconductor heterojunctions, the electron transport between these two semiconductors is significantly affected [28]. Therefore, it is considered to introduce a semiconductor between these two to reduce the mismatch between them as much as possible. As an n-type wide bandgap semiconductor, In(OH)$_3$ has suitable conduction band (CB) (–0.93 V) and valence band (VB) (4.24 V) positions versus NHE. It has a strong redox ability, so it is a promising photocatalytic material [29,30]. For this reason, it is possible to consider building a SnO (110) - In(OH)$_3$ (220) - InP (200) or SnO (211) - In(OH)$_3$ (422) - InP (222) assembly to reduce inter-semiconductor lattice mismatch.

In this paper, a wide bandgap semiconductor SnO layer was deposited on the In(OH)$_3$/InP surface to construct a SnO/In(OH)$_3$/InP catalyst, which greatly improves the catalyst stability and activity by applying an anti-corrosion SnO layer and a In(OH)$_3$ transition layer. Depositing the precious metal Pt on the surface of the catalyst further accelerates its charge separation and transfer. The obtained Pt/SnO/In(OH)$_3$/InP exhibits a hydrogen production rate of 144.42 μmol/g in 3 h under visible light illumination without remarkable decay in the successive four cycle tests, which is 123 times higher than that of naked In(OH)$_3$/InP without any sacrifice reagent under visible irradiation. The In(OH)$_3$ transition layer remarkably reduces the crystal mismatch between SnO and InP and increases charge transfer. This work provides a new method to develop high efficiency and high stability photocatalysts made of III-V semiconductor materials.

2 Experimental section

2.1 Preparation of In(OH)$_3$/InP

An improved hydrothermal method is used to prepare In(OH)$_3$/InP catalyst [31]. Typically, 1.00 g and 1.09 g of $InCl_3$ and NaOH, respectively, are dissolved in 27.2 mL of water, into which, 1.24 g of hexadecyl trimethyl ammonium bromide (CTAB), 9 mL of *n*-hexanol and 2.72 mL of *n*-octane are added. After stirring for 60 min, it is put in a 50 mL reactor. Next, 0.54 g and 1.73 g of red phosphorus (P) and iodine element (I_2), respectively, are added. Then it is transferred to an autoclave which is maintained at 160°C for 24 h. In the end, it is cooled at room temperature, centrifuged and washed (xylene, ethanol, dilute hydrochloric acid (0.1 mol/L), and deionized water). The obtained product is dried at 60°C and is ready for the test.

2.2 Preparation of SnO/In(OH)$_3$/InP catalyst

The SnO/In(OH)$_3$/InP catalyst is prepared by the hydrothermal method. First, 200 mg of In(OH)$_3$/InP powder and a calculated amount of $SnCl_2 \cdot 2H_2O$ are added to the beaker, then 30 mL of water is added, after stirring for 30 min, 0.7 mol/L KOH is added, and the dispersion is stirred ultrasonically for 30 min. It is then transferred to an autoclave which is reacted at 80°C for 15 h. The resulting products were collected by filtering, and washed with water and ethanol, respectively. The powder is dried at 60°C to obtain the final product. The obtained samples are donated respectively according to the different ratios of SnO (3%, 5%, 7%, and 10%, respectively).

2.3 Photocatalytic activity and AQE measurement

The photocatalytic activities are tested in a quartz reactor (approximately 190 mL). The effective irradiation area of the reactor is 11.9 cm^2. For each run, 50 mg of SnO/In(OH)$_3$/InP powder is dispersed in water, and a calculated amount of H_2PtCl_6 solution (1% (mass fraction)) is added under stirring. Ar is bubbled for 20 min before the reaction. The photocatalytic activity is measured by gas chromatography (Agilent 6820, Ar support). The light source is 300 W Xenon lamp equipped with different wavelength optical cut-off filters. For comparison, In(OH)$_3$/InP and SnO are also tested under similar conditions.

To measure the AQE (apparent quantum efficiency), the different wavelength bandpass filters (440, 460, 490, 520, and 550 nm) are used. n_p is measured by a calibrated FU100 radiometer. The AQE of photocatalytic hydrogen production is calculated according to Eq. (1) without considering refraction and scattering loss of photons.

$$\mathrm{AQE}(\%) = \frac{2n_{H_2}}{n_p} \times 100, \tag{1}$$

where n_{H_2} is the production of hydrogen (μmol), and n_P is the number of incident photons (μmol^{-1}m^{-2}s^{-1}), $n_P = t \times S \times Q$ (t is the reaction time, S is the effective illumination area of the reactor, and Q is the number of incident photons measured by the radiometer).

2.4 Stability test

The stability of the catalyst is studied by successive reaction cycles under similar reaction conditions. After

each 3 h, the reaction solution is centrifuged, washed with water, and then re-dispersed in water for cyclic reaction. More detailed information for working electrode preparation, electrochemical measurements and sample characterization are presented in the Electronic Supplementary Material.

3 Results and discussion

3.1 Structure and morphology characterization

The XRD patterns of the prepared samples show typical distinct diffraction peaks, which can be ascribed to $In(OH)_3$, InP, and SnO (see Fig. 1 and Figs. S1–S2). A series of diffraction peaks centered at 22.2°, 31.6°, 35.5°, 39.0°, 45.4°, 51.1°, 56.4°, 66.8°, 70.8°, 75.3°, and 79.7° correspond to the (200), (220), (310), (222), (400), (420), (422), (440), (600), (620), and (622) planes of $In(OH)_3$ (PDF#16-0161) [32], while the peaks centered at 26.2°, 30.4°, 51.5° and 79.9° correspond to the (111), (200), (311), and (422) planes of InP sphalerite structure (PDF#65-0233) [33]. In addition, the typical peaks of SnO are well consistent with the standard card (PDF#06-0395) [34]. The XRD patterns of the SnO/$In(OH)_3$/InP and Pt/SnO/$In(OH)_3$/InP composite photocatalysts show similar diffraction peak characteristics as $In(OH)_3$/InP, indicating that the protective layer SnO and co-catalyst Pt do not change the crystal structure of the catalyst [35]. No obvious diffraction peak belonging to SnO is observed in XRD patterns due to the low loading of SnO in the prepared catalysts.

The microstructure and morphology of prepared SnO/$In(OH)_3$/InP catalyst are investigated using TEM (Fig. 2 (a)). The nanoparticles exhibit a typical aggregation due to the limited passivation during the hydrothermal reactions. In the HRTEM image of Fig. 2(b), three sets of ordered lattice structures show that the composite catalyst is constructed by the order of InP, $In(OH)_3$, and SnO. Moreover, the multi-group lattice spacing of 0.29, 0.27, and 0.26 nm can be respectively indexed to the InP (200), $In(OH)_3$ (220), and SnO (110) plane, indicating that the SnO/$In(OH)_3$/InP photocatalyst is successfully synthesized. The lattice fringes of InP, $In(OH)_3$, and SnO are 0.29, 0.27, and 0.26 nm respectively, indicating that the $In(OH)_3$ transition layer can reduce the lattice mismatch between SnO and InP. It accelerates the charge separation and transfer during the reaction process. The Pt/SnO/$In(OH)_3$/InP catalyst with tightly contacted interfaces shows similar morphological characteristics as SnO/$In(OH)_3$/InP (Fig. S3(a)). Many Pt particles with 0.18 nm lattice fringes are observed on the catalyst surface (Fig. S3(b)), indicating the co-catalyst Pt is well deposited on the catalyst. This consequence can be further proved by the elemental mapping images of Pt/SnO/$In(OH)_3$/InP due to relatively homogeneous element spots of In, P, Sn, O, and Pt (Fig. S4).

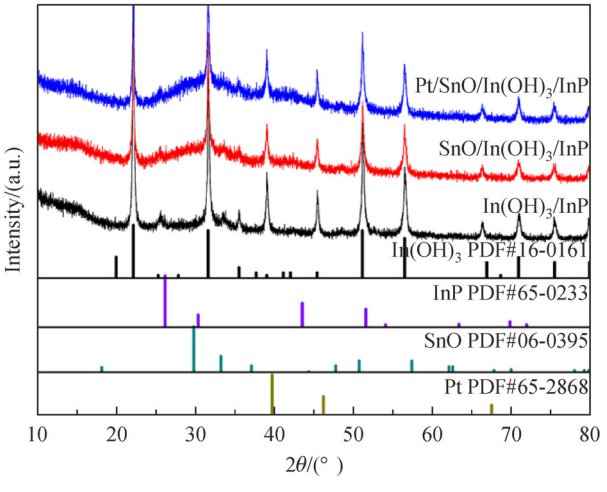

Fig. 1 X-ray diffraction (XRD) patterns of $In(OH)_3$/InP in different catalytic systems.

XPS is used to analyze the element chemical state of as-prepared catalysts. The survey XPS spectra of samples show typical Sn 3d, O 1S, In 3d, P 2P and Pt 4f peaks. No other peaks of impurities appeared (see the result in Figs. S5 and S6). Figure 3(a) shows clear peaks centered at 486.9 eV to 487.2 eV, which belong to typical characteristic Sn $3d_{5/2}$ peaks of SnO [36]. The O 1s peak shifts to the high energy side about 0.5 eV when SnO loaded onto $In(OH)_3$/InP, indicating the strong interaction between SnO and InP via hydroxide species. The In $3d_{5/2}$ peaks located at 444.7 eV and 445.2 eV, indicating In atom neighbored with P and O atoms, possibly as InP and In $(OH)_3$ like species [37–39]. Very clear P 2p peaks are observed, centered at 129.3 eV, 130.0 eV, and 133.2 eV, respectively. The former two peaks can be ascribed to the P in InP, the latter can be ascribed to the P neighbored with O (Fig. 3(d)) [40]. The Pt 4f centered at 72.6 eV indicates that the metallic Pt is located near the O atoms of SnO [41].

3.2 UV-vis diffuse reflection spectra

The light absorption properties of Pt/SnO/$In(OH)_3$/InP series photocatalysts are studied by utilizing the ultraviolet-visible absorption technique (Fig. 4). According to Fig. 4(a), the Pt/SnO/$In(OH)_3$/InP catalyst exhibits significantly enhanced light absorption and exhibits redshift of the absorption edge compared with $In(OH)_3$/InP and SnO/$In(OH)_3$/InP. It is known that SnO is a wide bandgap semiconductor (2.59 eV) and is transparent to visible light [42]. Coating SnO on catalyst surface will permit input light to reach InP and generate excited charges for the following reaction. The optical band gap of the prepared catalysts can be deduced from $\alpha h\upsilon = A(h\upsilon - E_g)^{n/2}$ according to the absorption spectra in Fig. 4(a) [43], where α is the absorption coefficient, $h\upsilon$ is the light energy, A is the constant, E_g is the optical band gap, and $n = 1$ [35]. The E_g of $In(OH)_3$/InP, SnO/$In(OH)_3$/InP, and Pt/SnO/$In(OH)_3$/

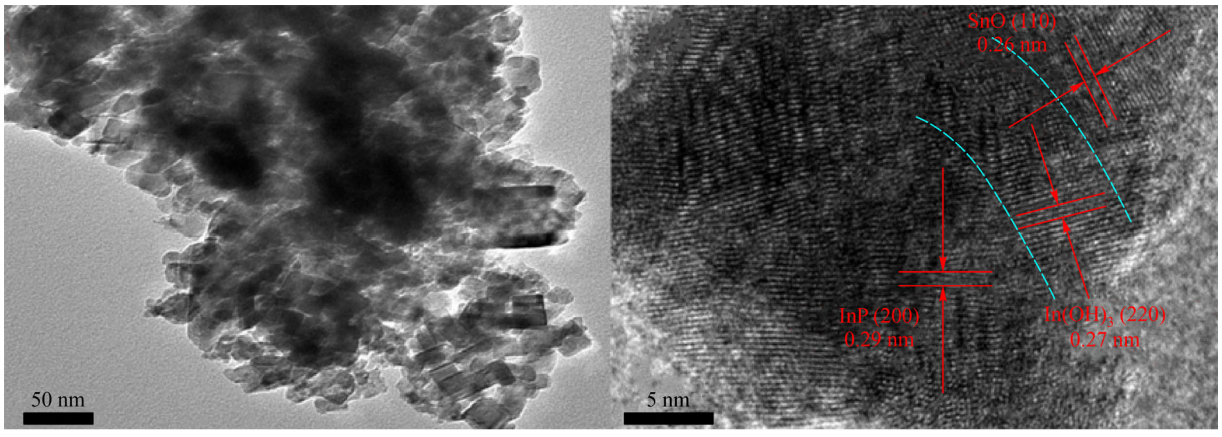

Fig. 2 Microstructure and morphology of prepared SnO/In(OH)$_3$/InP catalyst.
(a) TEM image; (b) HRTEM images of SnO/In(OH)$_3$/InP.

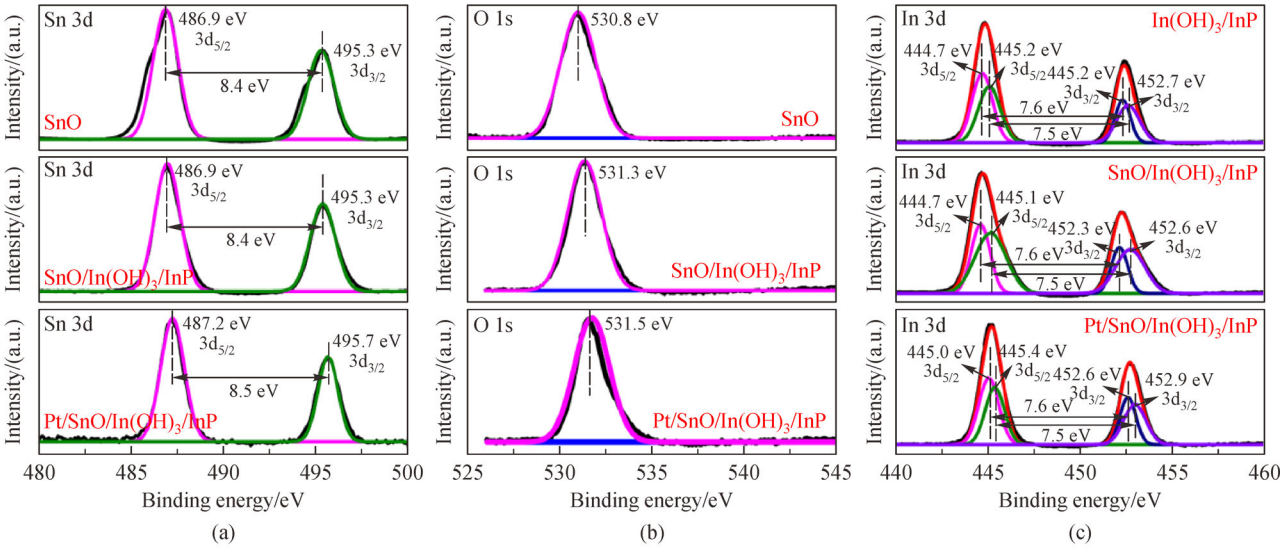

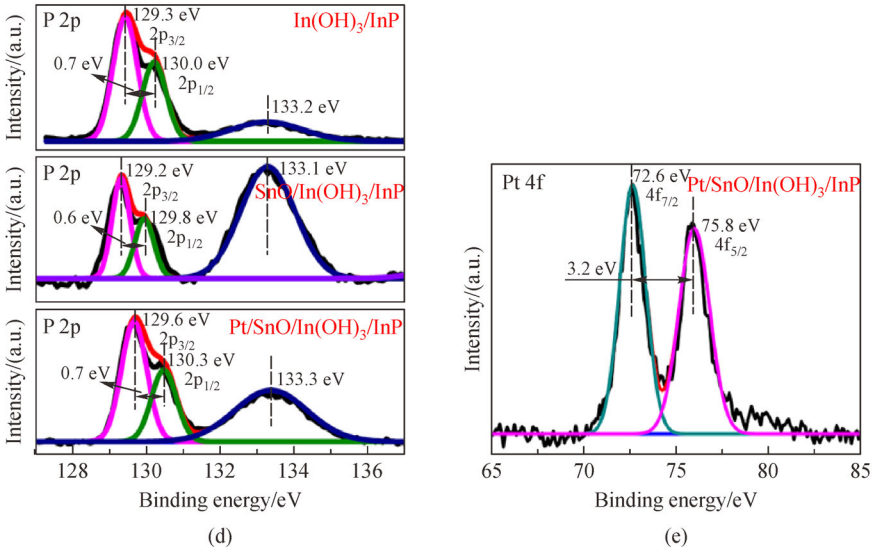

Fig. 3 X-ray photoelectron spectroscopy (XPS) spectra of In(OH)$_3$/InP based catalysts.
(a) Sn 3d; (b) O 1s; (c) In 3d; (d) P 2p; (e) Pt 4f.

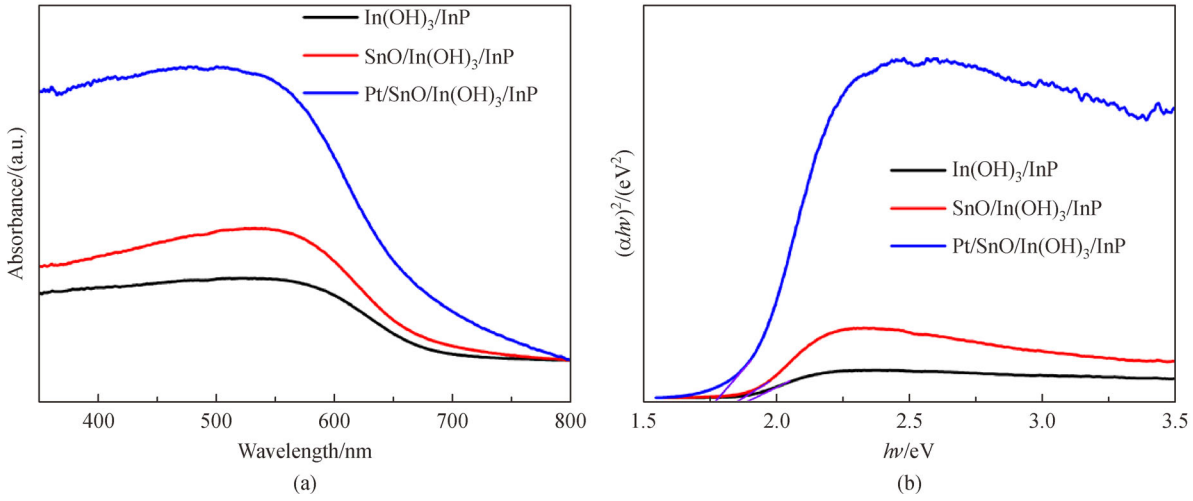

Fig. 4 Light absorption properties of Pt/SnO/$In(OH)_3$/InP series photocatalysts. (a) UV-vis absorption spectra; (b) band gap of $In(OH)_3$/InP based catalysts.

InP is approximately 1.90, 1.84, and 1.76 eV, respectively, indicating that the Pt/SnO/$In(OH)_3$/InP catalyst can absorb most of input light with a wavelength of up to 700 nm.

3.3 Photocatalytic activity and stability test

Figure 5 presents the activity results of catalysts for H_2 generation from water under visible light irradiation. The SnO sample exhibits a very low activity, while SnO/In$(OH)_3$/InP (3% (mass fraction) SnO) show a quite high activity for over-all water splitting to hydrogen and oxygen. The ratio of hydrogen to oxygen is nearly 2:1 (see the results in Fig. S7). Its activity is about twice higher than that of $In(OH)_3$/InP. Although the $In(OH)_3$/InP catalyst shows an initial activity for water splitting, it suffers corrosion. As mentioned later, its activity decays when the reaction is prolonged. The concentration of $(PO_4)^{3-}$ in all catalyst dispersion were measured after 7 h of reaction, and it was found the concentration of $(PO_4)^{3-}$ increased very significantly in $In(OH)_3$/InP catalyst dispersion (see the results in Fig. S8). After 7 h of reaction, the concentration of $(PO_4)^{3-}$ reached up to 5.0 μg/mL in the $In(OH)_3$/InP catalyst. Although this datum is lower than that of the InP catalyst (about 6.0 μg/mL), the results indicate that serious corrosion occurs both in $In(OH)_3$/InP and InP cases. However, after coating with SnO, only a trace amount of $(PO_4)^{3-}$ is detected, implying that the SnO coating could inhibit catalyst photocorrosion significantly. Consequently, the activity-dependence on the amount of SnO over SnO/$In(OH)_3$/InP catalyst (Fig. 6) was studied. When the SnO content increases from 3% to 10% (mass fraction), the activity is enhanced, but it decreases when SnO is overloaded. According to the stability tests of the multi-cycle test (see the results in Fig. 7), Pt/SnO/$In(OH)_3$/InP exhibits a very good stability and a high activity for

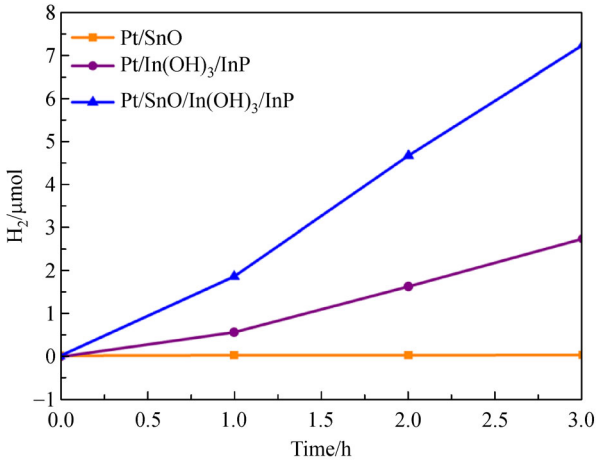

Fig. 5 Activities of photocatalytic H_2 generation over synthesized catalysts (⩾420 nm).

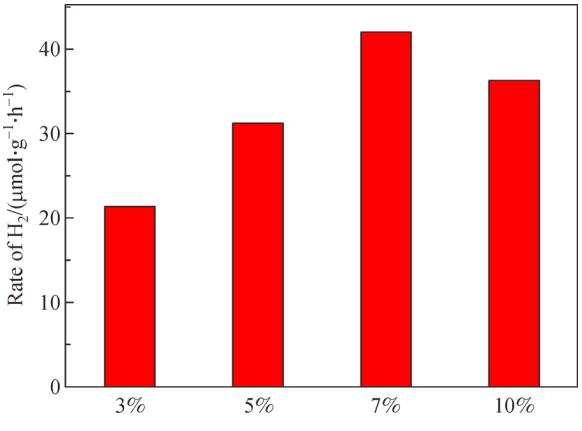

Fig. 6 Photocatalytic activity for H_2 evolution rate over SnO/$In(OH)_3$/InP catalyst at different SnO loading amounts (⩾420 nm).

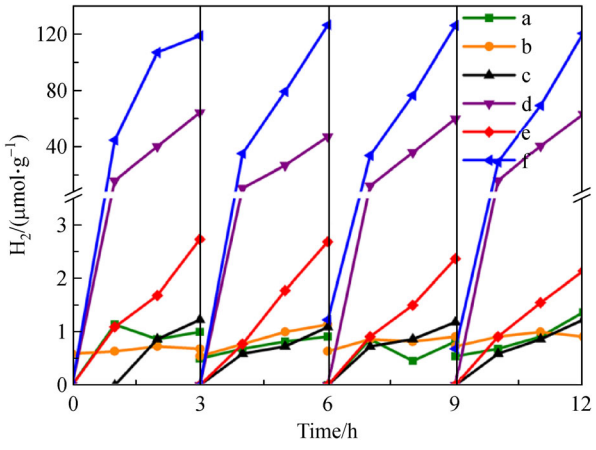

a–SnO; b–Pt/SnO; c–In(OH)$_3$/InP; d–Pt/In(OH)$_3$/InP; e–SnO/In(OH)$_3$/InP; f–Pt/SnO/In(OH)$_3$/InP

Fig. 7 Stability tests of different catalysts in multi-cycle reaction in pure water under visible light irradiation (⩾420 nm).

hydrogen generation in the successive cycle tests. After the fourth cycle test, that catalyst still gives 144.42 μmol/g of hydrogen in 3 h, which is almost the same compared to the hydrogen amount generated over fresh catalyst. The AQE of the Pt/SnO/In(OH)$_3$/InP photocatalyst were also measured under different wavelengths of visible light (Fig. 8).

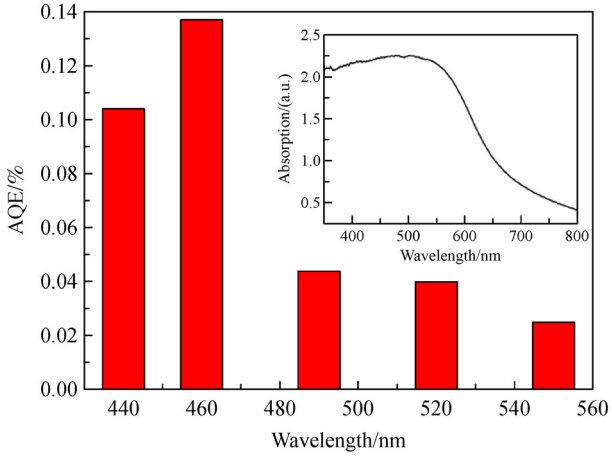

Fig. 8 Apparent quantum efficiencies of Pt/SnO/In(OH)$_3$/InP photocatalyst under different wavelength irradiation.

The hydrogen and oxygen production test of the Pt/SnO/In(OH)$_3$/InP catalyst in pure water is conducted under visible light irradiation. In Fig. S7, the hydrogen and oxygen production generate continuously from catalyst dispersion at a hydrogen to oxygen ratio of nearly 2:1. To further prove that the Pt/SnO/In(OH)$_3$/InP catalyst can decompose pure water photocatalytically, the isotope tracer experiment is performed. In Figs. 9(a) and 9(b), D_2 is detected ($m/z = 4$) when D_2O is used, and the signal of ($m/z = 36$) is detected when $H_2{}^{18}O$ is used.

3.4 Photoelectrochemical test

3.4.1 Photocurrent response

The photocurrents of synthesized samples are tested, whose results are presented in Fig. 10. The photocurrent density is closely connected with the applied bias voltage [44]. According to the results, Pt/SnO/In(OH)$_3$/InP present the highest photocurrent both at 0 V and 1.23 V (RHE), which is about three times higher than that of the SnO/In(OH)$_3$/InP sample at 1.23 V (RHE). The results indicate that coating SnO significantly enhances the separation and transfer of charges in a composite photocatalyst.

3.4.2 PL and TRPL

The synthesized samples are further studied by photoluminescence (PL) and time-resolved photoluminescence (TRPL) (see Fig. 11). According to the results in Fig. 11(a), In(OH)$_3$/InP presents a strong photoluminescence emission peak centered at 797 nm under 532 nm excitation. Once the In(OH)$_3$/InP is coated by SnO, the PL emission density is significantly decreased, indicating that the recombination of excited charges is remarkably inhibited. If the sample is further coated by the Pt particle, the PL emission density decreases, which might be caused by the charge transfer enhancement over catalyst by Pt loading. The time-resolved photoluminescence technique is used to get the lifetimes of synthesized samples, and the results are given in Fig. 11(b) and Table S1. The average photoluminescence lifetime of charges in different catalysts are quite different. Accordingly, the data of In(OH)$_3$/InP, Pt/In(OH)$_3$/InP and Pt/SnO/In(OH)$_3$/InP catalysts are 0.050 ns, 0.061 ns, and 0.068 ns, respectively. Among them, the lifetime of photogenerated electrons of the Pt/In(OH)$_3$/InP and SnO/In(OH)$_3$/InP catalysts is shorter than that of the Pt/SnO/In(OH)$_3$/InP catalysts, mainly due to the introduction of SnO and precious metal. Pt accelerates the migration of photogenerated carriers and makes electron-hole pairs effectively separate, so that the catalyst exhibits an excellent photocatalytic activity.

3.4.3 CV and LSV

Figure 12(a) gives a linear scan of the In(OH)$_3$/InP, SnO/In(OH)$_3$/InP, Pt/In(OH)$_3$/InP, and Pt/SnO/In(OH)$_3$/InP photocatalysts. The current intensity of each catalyst increases with the applied bias, indicating that the prepared samples are typical n-type semiconductors [45]. The Pt/SnO/In(OH)$_3$/InP photocatalyst has a stronger current density than In(OH)$_3$/InP, SnO/In(OH)$_3$/InP, Pt/In(OH)$_3$/InP.

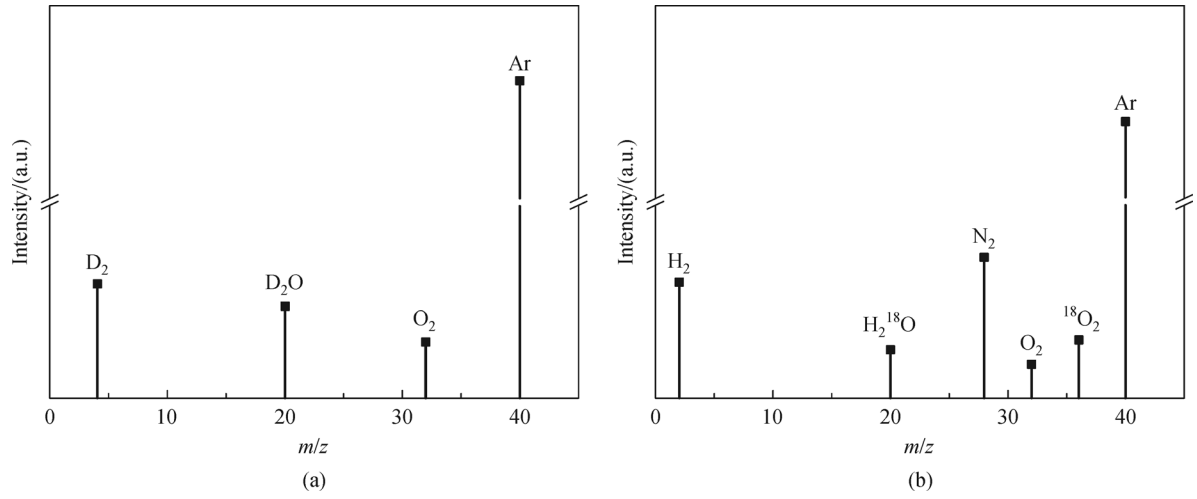

Fig. 9 GC-MS signals of gas generated over Pt/SnO/In(OH)$_3$/InP photocatalyst from water splitting.
(a) D_2O; (b) $H_2{}^{18}O$.

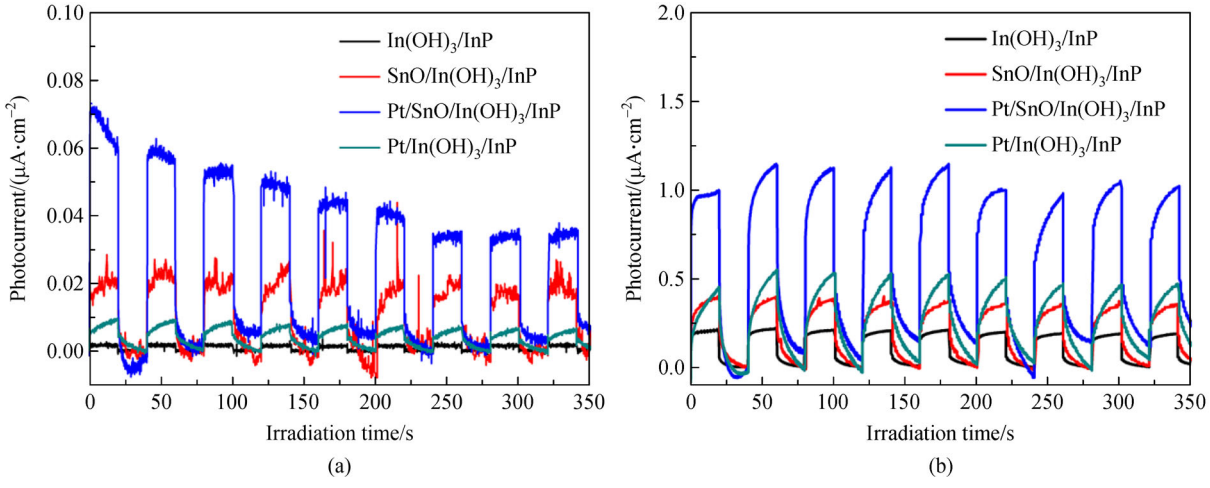

Fig. 10 Photocurrent of synthesized photocatalysts.
(a) 0 V (versus RHE); (b) 1.23 V (versus RHE).

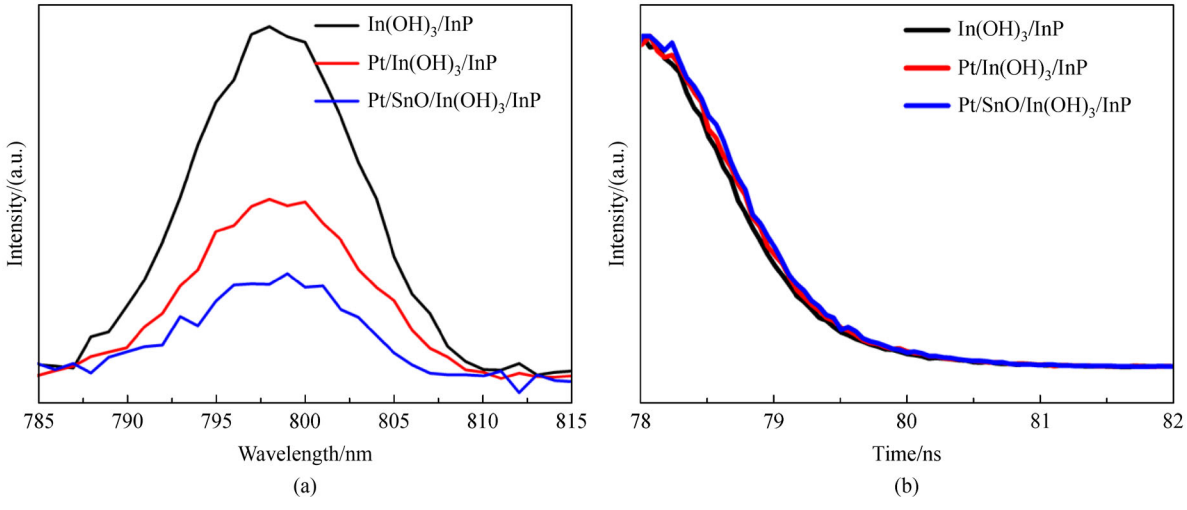

Fig. 11 Fluorescence spectra of In(OH)$_3$/InP based catalysts.
(a) Steady-state fluorescence spectra; (b) time-resolved fluorescence spectra.

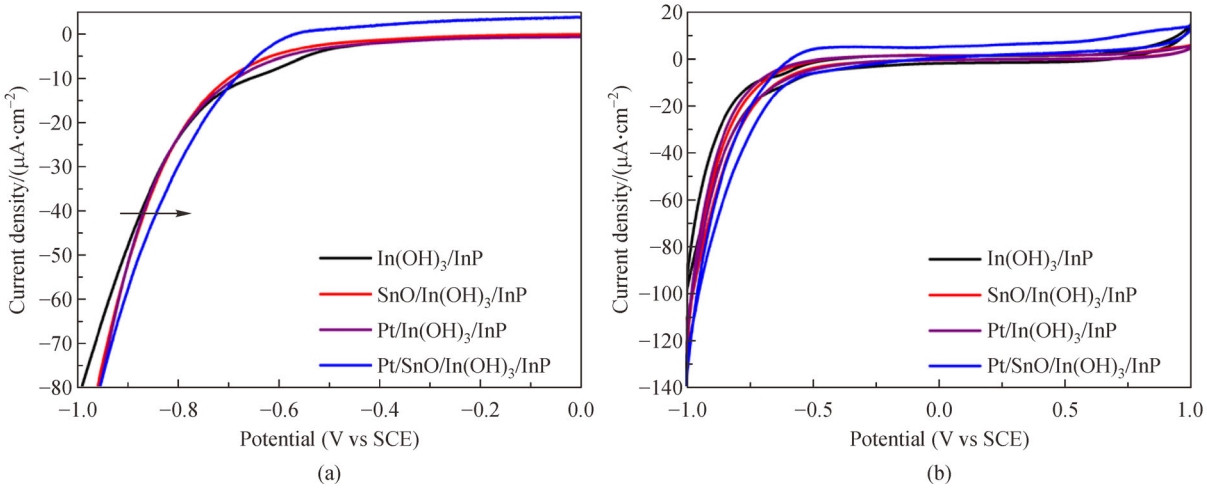

Fig. 12 Electrochemical responses of In(OH)$_3$/InP based catalysts.
(a) LSV curves; (b) cyclic voltammograms.

In addition, CV is also used to study the photoelectrochemical performance of the photocatalyst. As shown in Fig. 12(b), the current density of the Pt/SnO/In(OH)$_3$/InP electrode is larger than that of In(OH)$_3$/InP, SnO, and SnO/In(OH)$_3$/InP, indicating that the electron transfer rate is significantly improved on Pt/SnO/In(OH)$_3$/InP.

3.4.4 Mott-Schottky analysis

To measure the flat band potential of catalysts, Mott-Schottky analysis is performed (Fig. 13). InP is a typical p-type semiconductor [31]. According to Fig. 13, the flat band potential of In(OH)$_3$/InP is −1.10 V versus SCE. The corresponding standard hydrogen electrode potential can be calculated according to Nernst equation [46], expressed as

$$E_{FB}(\text{versus NHE}) = E_{FB}(\text{SCE}) + E_{SCE} + 0.059\,\text{pH}, \quad (2)$$

where E_{FB} is flat band potential, the pH value of the electrolyte is about 7, and E_{SCE} = 0.24 V. The calculated E_{FB} of the catalyst is –0.45 V versus NHE. The calculated CB and VB of the catalyst are –0.55 V and 0.88 V versus NHE, respectively. Based on the Hall effect test results (Table S2), SnO is a p-type semiconductor [34]. The E_{FB} of SnO/In(OH)$_3$/InP and Pt/SnO/In(OH)$_3$/InP shifts downside due to the formation of heterojunction.

3.5 *I-V* curve

To measure the conductivity of the catalyst, the *I-V* test is conducted. The *I-V* curve of the sample (Fig. 14) indicates that the catalyst Pt/SnO/In(OH)$_3$/InP presents the best conductivity compared with In(OH)$_3$/InP and SnO/In(OH)$_3$/InP [47], which is also in good agreement with activity dependence. At the same time, when the voltage is

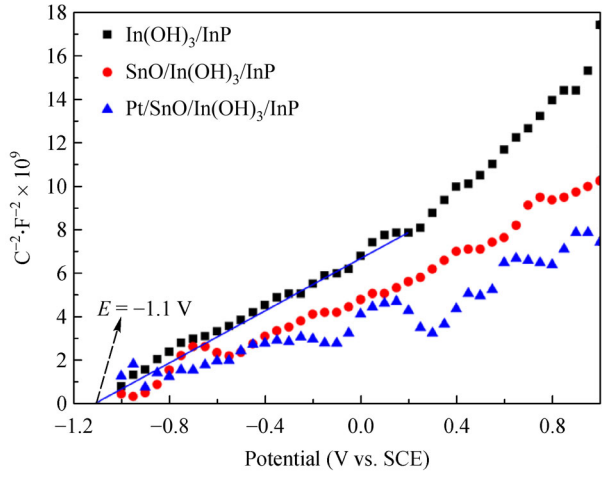

Fig. 13 Mott-Schottky images of In(OH)$_3$/InP based catalysts.

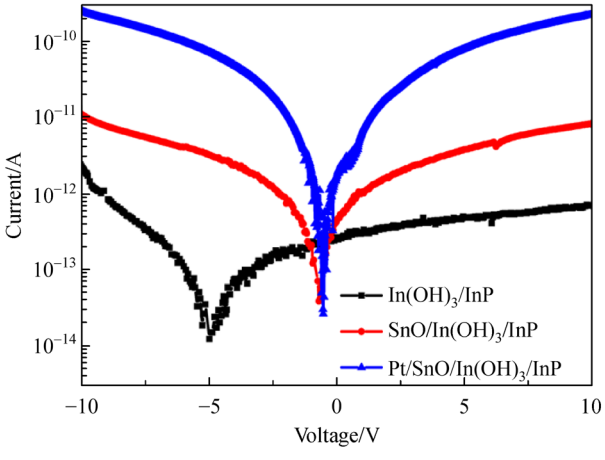

Fig. 14 *I-V* characteristics of In(OH)$_3$/InP in different catalysts.

scanned from –10V to 10V, the current curve of $In(OH)_3$/InP will fluctuate and shift dramatically, possibly due to the high resistance of $In(OH)_3$/InP and defects in the material itself [48].

3.6 Photocatalytic mechanism

Based on the above results and analysis, a possible photocatalytic mechanism of Pt/SnO/$In(OH)_3$/InP photocatalyst for water splitting is proposed (Fig. 15). When the p-type SnO is coated on $In(OH)_3$/InP, the Fermi level of n-type $In(OH)_3$/InP decreases until it reaches an equilibrium state on p-n heterojunction crystal interface and establishes a built-in electric field between the SnO and $In(OH)_3$ [49]. Under the irradiation of visible light, SnO and InP simultaneously generate electrons and holes [31,34]. At the same time, the $In(OH)_3$ with a wide bandgap cannot be excited under visible light, and it can only be used as a transition layer to transfer electrons because the CB of catalysts decreases in the order of SnO > $In(OH)_3$ > InP. The photogenerated electrons are transferred from the CB of SnO to the CB of $In(OH)_3$, and then to the CB of InP. Finally, Pt acts as an electron capture center, capturing photo-generated electrons and catalyzing protons to generate H_2. Because the valence band position of $In(OH)_3$ is much lower than that of SnO and InP, most of the holes still remain in SnO and InP. As a consequence, the separation and transfer of electrons and holes are realized. Then the holes in SnO oxidize H_2O to generate O_2. Moreover, the $In(OH)_3$ transition layer can effectively reduce the lattice matching between the SnO and InP, accelerating the transfer of photo-generated charge. The SnO anti-corrosion layer can effectively suppress the photocorrosion of $In(OH)_3$ and InP because it blocks the direct contact of the catalysts from water. Therefore, the $In(OH)_3$ transition layer and the SnO anti-corrosion layer accelerate the separation and transfer of charges and suppress the photocorrosion of the catalyst, improving the photocatalytic activity.

4 Conclusions

In summary, this study successfully constructs the SnO/$In(OH)_3$/InP system by utilizing the two-step hydrothermal method. The anti-corrosion SnO layer and the $In(OH)_3$ transition layer can effectively improve the stability and activity of the photocatalyst, thereby reducing the crystal mismatch between SnO and InP and increasing the charge transfer. The further introduction of the precious metal Pt accelerates its charge separation and transfer. The obtained Pt/SnO/$In(OH)_3$/InP photocatalyst, under visible light irradiation without adding any electron donor, has a hydrogen production rate of 144.42 μmol/g within 3 h, which is 123 times higher than that of bare InP without obvious decay.

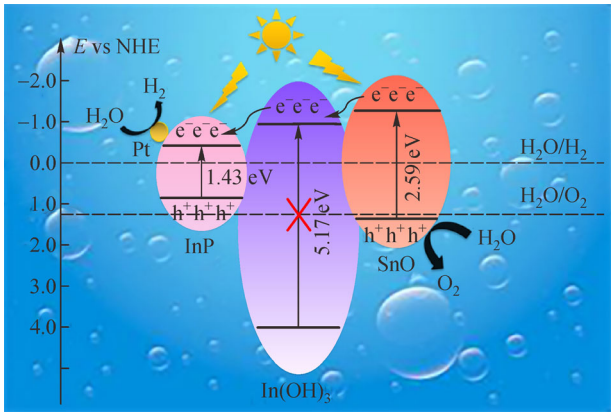

Fig. 15 Mechanism of Pt/SnO/$In(OH)_3$/InP photocatalyst for photocatalytic water splitting ($\lambda \geqslant 420$ nm).

Electronic Supplementary Material Supplementary material is available in the online version of this article at https://doi.org/10.1007/s11708-021-0764-x and is accessible for authorized users.

References

1. Kamat P V. Energy outlook for planet earth. Journal of Physical Chemistry Letters, 2013, 4(10): 1727–1729
2. Wang Y, Chen J, Zhang X, et al. Effects of different linear diamines on the performance of photocatalysts for hydrogen production of sensitized graphene. Journal of Molecular Catalysis (China), 2020, 34(1): 1–7 (in Chinese)
3. Dinga G P. Hydrogen: the ultimate fuel and energy carrier. International Journal of Hydrogen Energy, 1989, 14(11): 777–784
4. Kamat P V. Meeting the clean energy demand: nanostructure architectures for solar energy conversion. Journal of Physical Chemistry C, 2007, 111(7): 2834–2860
5. Wang M, Ma J, Lu G. The inhibition of hydrogen and oxygen recombination reverse reaction on cocatalyst surface in photocatalytic overall water splitting for hydrogen evolution. Journal of Molecular Catalysis (China), 2019, 33(5): 461–485 (in Chinese)
6. Lewis N S. Introduction: solar energy conversion. Chemical Reviews, 2015, 115(23): 12631–12632
7. Sun G, Mao S, Ma D, et al. One-step vulcanization of Cd(OH)Cl nanorods to synthesize CdS/ZnS/PdS nanotubes for highly efficient photocatalytic hydrogen evolution. Journal of Materials Chemistry A, Materials for Energy and Sustainability, 2019, 7(25): 15278–15287
8. Xiao S, Dai W, Liu X, et al. Microwave-induced metal dissolution synthesis of core-shell copper nanowires/ZnS for visible light photocatalytic H_2 evolution. Advanced Energy Materials, 2019, 9(22): 1900775
9. Peng L, Liu Y, Li Y, et al. Fluorine-assisted structural engineering of colloidal anatase TiO_2 hierarchical nanocrystals for enhanced photocatalytic hydrogen production. Nanoscale, 2019, 11(46): 22575–22584
10. Wang L, Tsang C S, Liu W, et al. Disordered layers on WO_3 nanoparticles enable photochemical generation of hydrogen from

water. Journal of Materials Chemistry A, Materials for Energy and Sustainability, 2019, 7(1): 221–227
11. Feng Y, Wang Y, Li M, et al. Novel visible light induced Ag_2S/g-C_3N_4/ZnO nanoarrays heterojunction for efficient photocatalytic performance. Applied Surface Science, 2018, 462: 896–903
12. Dong B, Cui J, Gao Y, et al. Heterostructure of 1D Ta_3N_5 nanorod/$BaTaO_2N$ nanoparticle fabricated by a one-step ammonia thermal route for remarkably promoted solar hydrogen production. Advanced Materials, 2019, 31(15): 1808185
13. Shi X, Li H, Zhao H. Solid-state z-scheme photocatalytic systems to splitting water and photo-reduce carbon dioxide. Journal of Molecular Catalysis (China), 2019, 33(4): 391–397
14. Hojamberdiev M, Khan M M, Kadirova Z, et al. Synergistic effect of g-C_3N_4, $Ni(OH)_2$ and halloysite in nanocomposite photocatalyst on efficient photocatalytic hydrogen generation. Renewable Energy, 2019, 138: 434–444
15. Geng M, Peng Y, Zhang Y, et al. Hierarchical $ZnIn_2S_4$: a promising cocatalyst to boost visible-light-driven photocatalytic hydrogen evolution of $In(OH)_3$. International Journal of Hydrogen Energy, 2019, 44(12): 5787–5798
16. Luo J, Zhang S, Sun M, et al. A critical review on energy conversion and environmental remediation of photocatalysts with remodeling crystal lattice, surface, and interface. ACS Nano, 2019, 13(9): 9811–9840
17. Jin X, Shao Y, Zhen Y, et al. Progress in modification of strontium titanate photocatalyst. Journal of Molecular Catalysis (China), 2020, 34(6): 559–568 (in Chinese)
18. Sunkara S, Sunkara M, Garcia A, et al. New III–V semiconductor alloys for solar hydrogen production. In: 228th Electrochemical Society Meeting, Phoenix, USA, 2015
19. Lou P, Lee J Y. GeC/GaN vdW heterojunctions: a promising photocatalyst for overall water splitting and solar energy conversion. ACS Applied Materials & Interfaces, 2020, 12(12): 14289–14297
20. Li P, Xiong T, Sun S, Chen C. Self-assembly and growth mechanism of N-polar knotted GaN nanowires on c-plane sapphire substrate by Au-assisted chemical vapor deposition. Journal of Alloys and Compounds, 2020, 825: 154070
21. Wilhelm T S, Soule C W, Baboli M A, et al. Fabrication of suspended III–V nanofoils by inverse metal-assisted chemical etching of $In_{0.49}Ga_{0.51}P$/GaAs heteroepitaxial films. ACS Applied Materials & Interfaces, 2018, 10(2): 2058–2066
22. Joyce H J, Wong-Leung J, Yong C K, et al. Ultralow surface recombination velocity in InP nanowires probed by terahertz spectroscopy. Nano Letters, 2012, 12(10): 5325–5330
23. Tournet J, Lee Y, Karuturi S K, Tan H H, et al. III–V semiconductor materials for solar hydrogen production: status and prospects. ACS Energy Letters, 2020, 5(2): 611–622
24. Li X, Lv X, Li N, et al. One-step hydrothermal synthesis of high-percentage 1T-phase MoS_2 quantum dots for remarkably enhanced visible-light-driven photocatalytic H_2 evolution. Applied Catalysis B: Environmental, 2019, 243: 76–85
25. Bang J, Das S, Yu E J, et al. Controlled photoinduced electron transfer from InP/ZnS quantum dots through Cu doping: a new prototype for the visible-light photocatalytic hydrogen evolution reaction. Nano Letters, 2020, 20(9): 6263–6271
26. Yu S, Xie Z, Ran M, et al. Zinc ions modified InP quantum dots for enhanced photocatalytic hydrogen evolution from hydrogen sulfide. Journal of Colloid and Interface Science, 2020, 573: 71–77
27. Kaizra S, Bellal B, Louafi Y, et al. Improved activity of SnO for the photocatalytic oxygen evolution. Journal of Saudi Chemical Society, 2018, 22(1): 76–83
28. Ryang Wie C. High resolution X-ray diffraction characterization of semiconductor structures. Materials Science and Engineering: R: Reports, 1994, 13(1): 1–56
29. Guo J, Ouyang S, Kako T, et al. Mesoporous $In(OH)_3$ for photoreduction of CO_2 into renewable hydrocarbon fuels. Applied Surface Science, 2013, 280: 418–423
30. Zhao Q, Li H, Cao Y. Effect of $In(OH)_3$ species modified ZnS on improved photocatalytic activity of photoreduction of CO_2. Journal of Solid State Chemistry, 2021, 296: 121976
31. Li P, Sui X, Xu J, et al. Worm-like InP/TiO_2 NTs heterojunction with unmatched energy band photo-enhanced electrocatalytic reduction of CO_2 to methanol. Chemical Engineering Journal, 2014, 247: 25–32
32. Motta F V, Marques A P A, Li M S, et al. Preparation and photoluminescence characteristics of $In(OH)_3$: xTb^{3+} obtained by microwave-assisted hydrothermal method. Journal of Alloys and Compounds, 2013, 553: 338–342
33. Nedeljković J M, Mićić O I, Ahrenkiel S P, et al. Growth of InP nanostructures via reaction of indium droplets with phosphide ions: synthesis of InP quantum rods and InP – TiO_2 composites. Journal of the American Chemical Society, 2004, 126(8): 2632–2639
34. Cui Y, Wang F, Iqbal M Z, et al. Synthesis of novel 3D SnO flower-like hierarchical architectures self-assembled by nano-leaves and its photocatalysis. Materials Research Bulletin, 2015, 70: 784–788
35. Tian B, Gao W, Zhang X, et al. Water splitting over core-shell structural nanorod CdS@Cr_2O_3 catalyst by inhibition of H_2-O_2 recombination via removing nascent formed oxygen using per-fluorodecalin. Applied Catalysis B: Environmental, 2018, 221: 618–625
36. Hien V X, Lee J H, Kim J J, et al. Structure and NH_3 sensing properties of SnO thin film deposited by RF magnetron sputtering. Sensors and Actuators B, Chemical, 2014, 194: 134–141
37. Li T, Wei H, Liu T, et al. Achieving efficient CO_2 electrochemical reduction on tunable in $(OH)_3$-coupled Cu_2O-derived hybrid catalysts. ACS Applied Materials & Interfaces, 2019, 11(25): 22346–22351
38. Zai J, Zhu J, Qi R, et al. Nearly monodispersed $In(OH)_3$ hierarchical nanospheres and nanocubes: tunable ligand-assisted synthesis and their conversion into hierarchical In_2O_3 for gas sensing. Journal of Materials Chemistry A, Materials for Energy and Sustainability, 2013, 1(3): 735–745
39. Jang E, Kim Y, Won Y H, et al. Environmentally friendly InP-based quantum dots for efficient wide color gamut displays. ACS Energy Letters, 2020, 5(4): 1316–1327
40. Li Q, Zhang J, Dai K, et al. *In-situ* synthesis of Au decorated InP nanopore arrays for enhanced photoelectrochemical hydrogen production. Journal of Alloys and Compounds, 2019, 774: 610–617
41. Yu J, Qi L, Jaroniec M. Hydrogen production by photocatalytic water splitting over Pt/TiO_2 nanosheets with exposed (001) facets. Journal of Physical Chemistry C, 2010, 114(30): 13118–13125

42. Sinha A K, Manna P K, Pradhan M, et al. Tin oxide with a p–n heterojunction ensures both UV and visible light photocatalytic activity. RSC Advances, 2014, 4(1): 208–211
43. Ning X, Zhen W, Wu Y, et al. Inhibition of CdS photocorrosion by Al_2O_3 shell for highly stable photocatalytic overall water splitting under visible light irradiation. Applied Catalysis B: Environmental, 2018, 226: 373–383
44. Cheng X, Zhang Y, Bi Y. Spatial dual-electric fields for highly enhanced the solar water splitting of TiO_2 nanotube arrays. Nano Energy, 2019, 57: 542–548
45. Smiri B, Saidi F, Mlayah A, et al. Effect of substrate polarity on the optical and vibrational properties of (311) A and (311) B oriented InAlAs/InP heterostructures. Physica E, Low-Dimensional Systems and Nanostructures, 2019, 112: 121–127
46. Gooch J W. Nernst equation. In: Encyclopedic Dictionary of Polymers. New York, NY: Springer New York, 2011: 909–909
47. Ning X, Li J, Yang B, et al. Inhibition of photocorrosion of CdS via assembling with thin film TiO_2 and removing formed oxygen by artificial gill for visible light overall water splitting. Applied Catalysis B: Environmental, 2017, 212: 129–139
48. Ghimire S, Dho J. Current–voltage characteristics and photovoltaic effect of a Au/$ZnFe_2O_4$/GaN Schottky junction. Journal of Physics D, Applied Physics, 2021, 54(9): 095103
49. Moniz S J A, Shevlin S A, Martin D J, et al. Visible-light driven heterojunction photocatalysts for water splitting – a critical review. Energy & Environmental Science, 2015, 8(3): 731–759